Simulation and optimization of a 6H-SiC metal–semiconductor–metal ultraviolet photodetector*

Chen Bin(陈斌)†, Yang Yintang(杨银堂), Li Yuejin(李跃进), and Liu Hongxia(刘红霞)

(Key Laboratory of the Ministry of Education for Wide Band-Gap Semiconductor Materials and Devices, School of Microelectronics, Xidian University, Xi'an 710071, China)

Abstract: Based on thermionic emission theory, a model of a 6H-SiC metal–semiconductor–metal (MSM) ultraviolet photodetector is established with the simulation package ISE-TCAD. A device with 3 μm electrode width (W) and 3 μm electrode spacing (L) is simulated. The findings show that the MSM photodetector has quite a low dark current of 15 pA at 10 V bias and the photocurrent is two orders of magnitude higher than the dark current. The influences of different structures on dark and illuminated current–voltage characteristics of the MSM photodetector are investigated to optimize the device parameters. Simulation results indicate that the maximum photocurrent and the highest ratio of photocurrent to dark current at 15 V bias are 5.3 nA and 327 with device parameters of W = 6 μm, L = 3 μm and W = 3 μm, L = 6 μm, respectively.

Key words: MSM structure; ultraviolet photodetector; Schottky contact; I–V characteristics
DOI: 10.1088/1674-4926/31/6/064010 **PACC:** 0670D; 0762; 7820

1. Introduction

In recent years, much research has been focused on high performance ultraviolet (UV) photodetectors. These detectors have a wide range of commercial and military applications, including ozone layer monitoring, space communications, flame detection, radiometry and analysis[1, 2]. Specifically, UV detection from flames can be used for applications ranging from solid-state detection for combustion control to detection of missile plumes. Radiometry applications can range from total dose UV monitoring for industrial processes to a UV detector for monitoring sun exposure. Analysis applications include air quality monitoring and UV spectroscopy. Silicon carbide (SiC) is a promising material for UV detectors. Due to the wide bandgap and high absorption coefficient in the UV region, the 6H-SiC UV photodetector has very low dark current, significantly high operating temperature and insensibility to visible/infrared ray background.

Up to now, some types of photodetectors have been proposed, such as Schottky diodes[3], p–n photodiodes[2], p–i–n photodiodes[4, 5], and metal–semiconductor–metal (MSM) diodes[6–9]. Among these structures, MSM UV detectors have attracted much interest due to their low intrinsic capacitance and high responsivity. However, the influence of the device structure on its performance is rarely studied, which limits the development of SiC MSM UV detectors.

In this paper, the working mechanism of a 6H-SiC MSM UV detector is studied with the two-dimensional simulation package ISE-TCAD. The effects of electrode width and spacing on dark current and photocurrent are investigated to obtain the optimum device structure, which is significant for design and fabrication of 6H-SiC MSM UV photodetectors.

2. Structure and model

2.1. Structure

The MSM UV detector is a two terminal device consisting of two Schottky barriers connected back to back. As shown in Fig. 1, the developed MSM detectors employ interdigitated finger patterns deposited on an epitaxial layer, in which one pad and the associated fingers form the anode and the other forms the cathode. The thickness and doping concentration of the n type 6H-SiC epitaxial layer are 3 μm and 3×10^{15} cm^{-3}, respectively. Au is selected as the Schottky contact electrode. The width and spacing of the finger electrode are both 3 μm, similar to a device previously reported in Ref. [9].

2.2. Model

In order to simulate the dark and illuminated current–voltage (I–V) characteristics of the MSM UV photodetector, the mobility model, recombination model, thermionic emission model, optical generation and absorption model are adopted. By solving the Poisson equation, current-continuity equations for electron and hole and the current density equa-

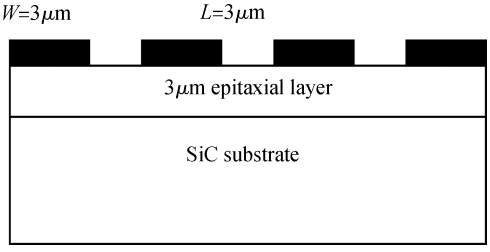

Fig. 1. Cross section of a typical 6H-SiC MSM UV detector.

* Project supported by the Pre-Research Foundation from the National Ministries and Commissions, China (Nos. 51323040118, 513080302).
† Corresponding author. Email: xidianchenbin@163.com
Received 15 September 2009, revised manuscript received 22 January 2010

tion, the electric potential distribution and carrier distribution before and after UV illumination are obtained. The Poisson equation and current-continuity equations used in the present model can be expressed as

$$\begin{cases} \nabla^2\phi = -\dfrac{\rho(x,y,z)}{\varepsilon}, \\ \dfrac{\partial n}{\partial t} = G_{\rm n} - U_{\rm n} + \dfrac{1}{q}\nabla\cdot J_{\rm n}, \\ \dfrac{\partial p}{\partial t} = G_{\rm p} - U_{\rm p} - \dfrac{1}{q}\nabla\cdot J_{\rm p}, \end{cases} \tag{1}$$

where n and p are electron and hole densities respectively, ϕ is the potential, $\rho(x, y, z)$ the charge density, J the current density, U the recombination rate, G the generation rate, and subscript n or p denotes electron or hole respectively. Current density is described by drift and diffusion of carriers, the current densities for electrons and holes are written as

$$\begin{aligned} J_{\rm n} &= qn\mu_{\rm n}E + qD_{\rm n}\nabla n, \\ J_{\rm p} &= qp\mu_{\rm p}E - qD_{\rm p}\nabla p. \end{aligned} \tag{2}$$

Here E is electrical field strength, μ is the carrier mobility and D is the diffusion coefficient. A more detailed description of the models mentioned above is given as follows.

2.2.1. Mobility model

The degradation of the mobility for impurity scattering is realized by the Masetti model. The model is expressed as[10]

$$\mu_{\rm dop} = \mu_{\rm min1}\exp\Big(\frac{-p_{\rm c}}{N_{\rm i}}\Big) + \frac{\mu_{\rm const}-\mu_{\rm min2}}{1+\Big(\dfrac{N_{\rm i}}{C_{\rm r}}\Big)^{\alpha}} - \frac{\mu_1}{1+\Big(\dfrac{C_{\rm s}}{N_{\rm i}}\Big)^{\beta}}, \tag{3}$$

where $N_{\rm i}$ denotes the total concentration of ionized impurities. $\mu_{\rm const}$ is determined by the constant mobility model[10]. $\mu_{\rm min1}$, $\mu_{\rm min2}$ and μ_1, as well as the reference doping concentrations $P_{\rm c}$, $C_{\rm r}$ and $C_{\rm s}$ and the exponents α and β are specified in Ref. [10].

2.2.2. Recombination model

The Shockley–Read–Hall recombination model is considered to describe the recombination in the course of photogenerated carrier transportation. The model is given by[10]

$$R_{\rm net}^{\rm SRH} = \frac{np - n_{\rm i,eff}^2}{\tau_{\rm p}(n+n_1)+\tau_{\rm n}(p+p_1)}, \tag{4}$$

$$n_1 = n_{\rm i,eff}\exp\frac{E_{\rm trap}}{kT}, \tag{5}$$

$$p_1 = n_{\rm i,eff}\exp\Big(-\frac{E_{\rm trap}}{kT}\Big), \tag{6}$$

where $E_{\rm trap}$ is the difference between the defect level and the intrinsic level. $n_{\rm i,eff}$ denotes effective intrinsic density. The minority lifetimes, $\tau_{\rm n}$ and $\tau_{\rm p}$, are modeled as a product of a doping dependent ($\tau_{\rm dop}$), a field dependent ($g_c(f)$) and a temperature dependent factor ($f(T)$). Lifetimes are written as

$$\tau_c = \tau_{\rm dop}[f(T)/(1+g_c(f))], \quad c = {\rm n, p}, \tag{7}$$

where $c = {\rm n}$ or $c = {\rm p}$ for electrons or holes.

2.2.3. Thermionic emission model

In our simulation, the thermionic emission model is taken into account to describe the hetero-junction interface between the metal and semiconductor. The model is given by[10]

$$J_{\rm n,2} = aq\Big[v_{\rm n,2}n_2 - \frac{m_2}{m_1}v_{\rm n,1}n_1\exp\Big(-\frac{\Delta E_{\rm c}}{K_{\rm B}T_{\rm e,1}}\Big)\Big]. \tag{8}$$

Here $a = 2$. $J_{\rm n,2}$ is the electron current density entering the metal and $J_{\rm n,1}$ is the electron current density leaving the semiconductor. Then $J_{\rm n,2}$ is equal to $J_{\rm n,1}$. The emission velocities are defined as

$$v_{{\rm n},i} = \sqrt{\frac{K_{\rm B}T_{{\rm e},i}}{2\pi m_i}}, \tag{9}$$

where $i = 1$ or 2 for the semiconductor or metal.

2.2.4. Optical generation and absorption model

Optical generation model is used to describe the generation of light inside and outside a device via vertical photon beams. The generation rate can be given by[10]

$$G^{\rm opt}(z,t) = J_0F_{\rm t}(t)F_{\rm xyv}\alpha(\lambda,z')\exp\Big[-\Big|\int_{Z_0}^{Z}\alpha(\lambda,z'){\rm d}z'\Big|\Big], \tag{10}$$

where J_0 denotes the incident beam intensity. $F_{\rm t}(t)$ is the beam time behavior function. $F_{\rm xyv}$ is equal to one inside the semiconductor and decreases to zero outside the semiconductor. Z_0 is the coordinate of the semiconductor surface. $\alpha(\lambda, z')$ is the absorption coefficient described as a function of wavelength and coordinates. $\alpha(\lambda, z')$ is dependent on the absorption model. The model is defined as[10]

$$\alpha(E_{\rm ph}) = \begin{cases} \alpha_1\exp[(E_{\rm ph}-E_1)/E_2], & E_{\rm ph} < E_1, \\ \alpha_1 + \alpha_2[(E_{\rm ph}-E_1)/E_2]^P, & E_{\rm ph} \geqslant E_1, \end{cases} \tag{11}$$

where $E_{\rm ph}$ is the photon energy and α_1, α_2, E_1, E_2, P are model parameters which can be specified in Ref. [10].

In addition, the incomplete ionization model[10] is considered in the device simulation which means the impurities are not completely ionized at room temperature or even higher temperatures. The barrier lowering model[10] is also used due to the effect of barrier lowering induced by image force.

3. Simulation and optimization

Based on the above models, the dark and illuminated I–V characteristics of the 6H-SiC MSM UV detector are investigated first with a numerical coupling algorithm and appropriate boundary conditions on a two-dimensional mesh. The influence of different structure on device performance is studied to obtain the optimum device structure.

3.1. Working mechanism of the 6H-SiC MSM UV photodetector

The dark and illuminated I–V characteristics are the most important characteristics of the detector, which are simulated with the structure in Fig. 1 and plotted in Fig. 2.

Ignoring the tunneling effect, material defects and other factors, we conclude that the dark current increases along with the increasing voltage. It is also clear that the dark current is

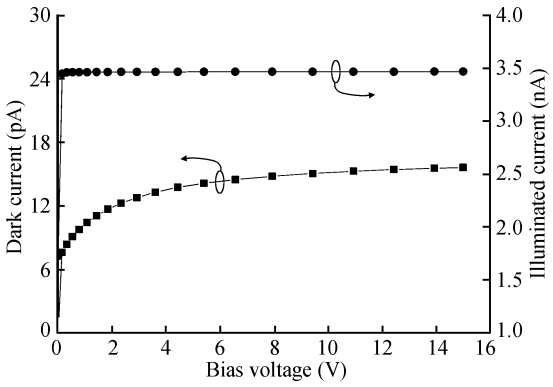

Fig. 2. Dark and illuminated I–V characteristics of the 6H-SiC UV detector with 3 μm width and 3 μm spacing.

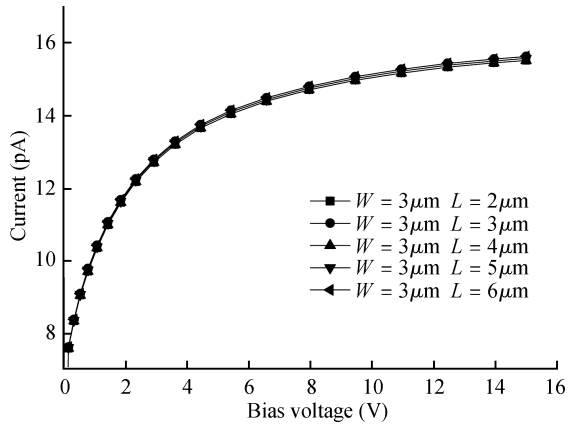

Fig. 3. Dark I–V characteristics of different finger spacings.

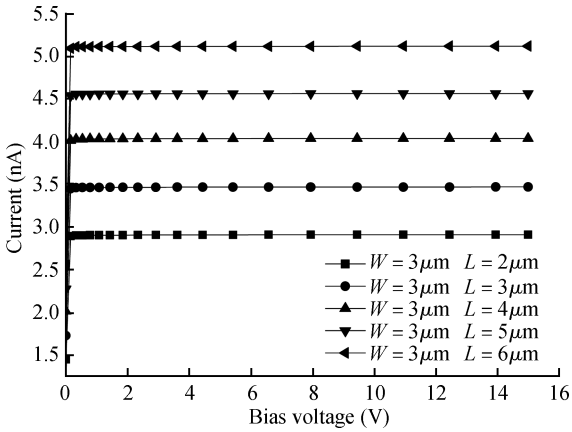

Fig. 4. Illuminated I–V characteristics of different finger spacings.

around 7 pA at the beginning, and then it increases slowly from 7 to 14 pA when the applied voltage increases from 0 to 5 V. Due to the reverse biased Schottky barrier lowering caused by image force at lower voltage, the dark current achieves saturation with a bias higher than 5 V.

Under illumination of 280 nm UV light, the photocurrent is 3.5 nA and the curve of the photocurrent is relatively flat. The ratio of the photocurrent to the dark current decreases with the increase of applied voltage, and the photocurrent is at least two orders of magnitude higher than the dark current. The results are consistent with experimental data and this proves the present model is reasonable. Actually, the photocurrent increases sharply under lower bias, then it tends to saturate. According to theoretical analysis of the MSM detector[11], the incomplete depletion in the depletion region under lower bias leads to the lack of photo-generated carriers and the low photocurrent. With the increase of voltage, the depletion width increases rapidly, which results in the steep increase of the photocurrent under lower bias. As the applied bias exceeds the reach-through voltage, the speed of the depletion region broadening decreases and the photocurrent increases slowly. When the voltage reaches the flat band voltage, the depletion region disappears. The device is totally reverse biased and the depletion width remains constant. As a result, the photocurrent achieves saturation.

3.2. Design of the detector

In the above analysis, the working principle of the detector is achieved. Then the performances of the detector with different structures are investigated and reasonable device structures are obtained.

3.2.1. Influence of finger spacing

Figure 3 shows a group of dark I–V characteristics for 6H-SiC MSM UV detectors with different metal spacings. It can be seen that these devices show a similar dark current around the 10^{-11}A level, which changes slightly with the increase of electrode spacing. According to thermionic emission theory, the dark current is proportional to the electrode area. So, electrode spacing is not the main factor affecting the dark I–V characteristics while electrode width remains constant.

The illuminated I–V characteristics for 6H-SiC MSM UV detectors are simulated under illumination at 280 nm, as shown in Fig. 4. We can clearly observe a much larger photocurrent of nA level with a lower bias. Also we see from this figure that the photocurrent of the device increases gradually from 2.9 to 5.1 nA while the electrode spacing changes from 2 to 6 μm. This change is due to the dependence of the photon-generation ratio on the photosensitive area. As the electrode width increases, the UV absorption region increases too. There are more photon-generated electron–hole pairs produced and collected under UV illumination. Meanwhile the SRH recombination rate changes slightly compared to that of photon generation rate so that they cause an increase in the illuminated current.

3.2.2. Influence of finger width

Figure 5 shows the dark I–V characteristics for 6H-SiC MSM UV detectors with different metal widths. The dark current increases rapidly from 9 to 26 pA when the metal width increases from 2 to 6 μm at 5 V applied voltage. Then, the dark current achieves saturation with the increase of applied bias. The maximum dark current is less than 30 pA at 15 V applied voltage. It is found that the variation of dark current shown in Fig. 5 is rather obvious, compared to a group of I–V curves shown in Fig. 3. These results indicate that the variation of metal electrode width has a more significant influence on dark I–V characteristics compared with changing the electrode spacing. One of the most important factors is that the elec-

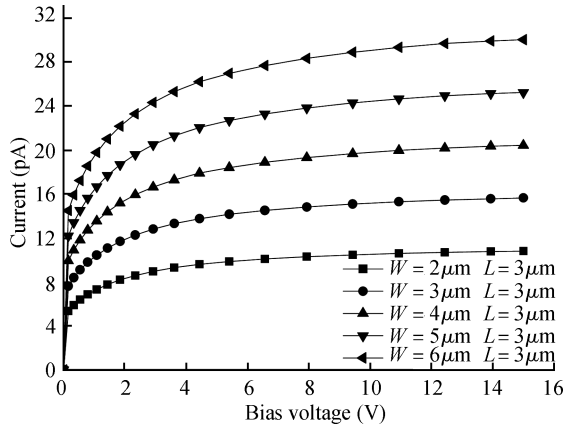

Fig. 5. Dark I–V characteristics of different finger widths.

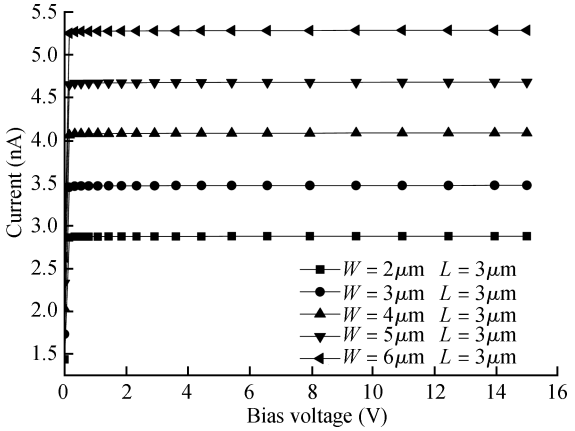

Fig. 6. Illuminated I–V characteristics of different finger widths.

trode area is changed directly due to the variation of electrode width.

By changing the contact metal width under UV illumination at 280 nm, we simulate the illuminated I–V characteristics for the 6H-SiC MSM UV detector shown in Fig. 6. The photocurrents plotted in Figs. 4 and 6 reach the nA level. There has been an obvious change of photocurrent with various device structures. The effects of various geometry sizes for the 6H-SiC MSM UV detector on illuminated I–V characteristics are different from those of dark I–V characteristics due to different working mechanisms for the photocurrent and dark current. The maximum photocurrent of a device with 6 μm electrode width and 3 μm metal spacing illustrated in Fig. 6 is 5.3 nA, larger than 5.1 nA which is the largest magnitude in Fig. 4 with a device parameter of 3 μm electrode width and 6 μm metal spacing.

3.2.3. Analysis and optimization of the detector

With the photocurrent simulation results presented in Figs. 4 and 6, we can draw two conclusions. The first is that the electric intensity under the metal electrodes is directly affected by electrode width. The wider the vertical electric distribution is, the better performance the device will possess. It is also found that electric intensity E under metal electrodes decreases rapidly due to the increase of vertical depth. Thus, the mobility velocity of photocarriers in the active area is limited and the time of electrode collecting carriers is greatly affected as well. For the planar MSM UV detector, electrons move under a weaker vertical electric field and its moving trace is curved, which indicates that a longer transit time is needed. Upon increasing the width of the metal electrode, the electric intensity under the electrode is increased and electrons move along an approximately straight line between two electrodes. Therefore, the transit time of the photo-generated carrier is reduced and effective photocurrent is promptly generated in the external circuit. The second conclusion is that the design of the metal electrode width W and spacing L is to minimize the incidence shadow effect and maximize the ratio of $L/(L + W)$.Thus, the device surface can obtain the maximum incident light. According to the principle above, L should be as large as possible. Photocurrents as shown in Figs. 4 and 6 have the same trend, which indicates that the photocurrent increases with the increase of metal electrode width and spacing. However, response speed or response time describes the transient behavior of photodetectors, which is associated with the structure of the device. The larger L is, the greater the response time will be. On the other hand, a wider metal width may cause a larger dark current due to the increase of electrode area. Therefore, we should make a trade-off between electrode width and spacing for optimization of the MSM UV detector.

Table 1. Ratio of photocurrent to dark current at 15 V bias.

Geometry size	$I_{\text{illumination}}/I_{\text{dark}}$
$W = 2\ \mu$m, $L = 3\ \mu$m	266
$W = 3\ \mu$m, $L = 3\ \mu$m	222
$W = 4\ \mu$m, $L = 3\ \mu$m	200
$W = 5\ \mu$m, $L = 3\ \mu$m	186
$W = 6\ \mu$m, $L = 3\ \mu$m	176
$W = 3\ \mu$m, $L = 2\ \mu$m	187
$W = 3\ \mu$m, $L = 4\ \mu$m	260
$W = 3\ \mu$m, $L = 5\ \mu$m	293
$W = 3\ \mu$m, $L = 6\ \mu$m	327

Table 1 lists the ratio of photocurrent to dark current at 15 V bias for various geometry sizes. We can clearly observe a much larger photocurrent to dark current contrast, which indicates that the ratios of photocurrent to dark current are larger than two orders of magnitude for all geometry sizes. The photocurrent of a device with 6 μm metal width and 3 μm metal spacing is the highest, whose photocurrent to dark current contrast is just 176 due to its larger dark current. The device with 3 μm metal width and 6 μm metal spacing achieves the largest ratio of photocurrent to dark current of 327.

4. Conclusions

To investigate the influences of geometry sizes on dark current and illuminated current, a model of a 6H-SiC MSM photodetector is established with the two-dimensional device simulation package ISE-TCAD. The results show that the 6H-SiC MSM photodetector has very low dark current and the ratio of photocurrent to dark current is larger than two orders of magnitude. Compared with the variation of electrode spacing, the variation of electrode width has a more important influence on the dark current of the 6H-SiC MSM photodetector. The device with 6 μm electrode width and 3 μm metal spacing achieves a maximum photocurrent of 5.3 nA. The highest ratio of pho-

tocurrent to dark current at 15 V bias is 327 with a device structure of 3 μm electrode width and 6 μm electrode spacing.

References

[1] Su Y K, Chang S J, Chen C H, et al. GaN metal–semiconductor –metal ultraviolet sensors with various contact electrodes. IEEE Sensors Journal, 2002, 2(4): 366

[2] Chen Q, Khan M A, Sun C J, et al. Visible-blind ultraviolet photodetectors based on GaN p–n junctions. Electron Lett, 1995, 31(20): 1781

[3] Chen Q, Yang J W, Osinsky A, et al. Schottky barrier detectors on GaN for visible-blind ultraviolet detection. Appl Phys Lett, 1997, 70(17): 2277

[4] Zhang Chunfu, Hao Yue, Zhang Jinfeng, et al. Model and simulation of GaN based PIN photodetectors. Chinese Journal of Semiconductors, 2005, 26(9): 1610

[5] You Da, Tang Yinwen, Zhao Degang, et al. Characteristics of a front-illuminated visible-blind UV photodetector based on GaN p–i–n photodiodes with high quantum efficiency. Chinese Journal of Semiconductors, 2006, 27(6): 896

[6] Chang P C, Yu C L, Chang S J, et al. High-detectivity nitride-based MSM photodetectors on InGaN–GaN multiquantum well with the unactivated Mg-doped GaN layer. IEEE J Quantum Electron, 2007, 43(11): 1060

[7] Kim D W, Chea K S, Park Y J, et al. Fabrication of metal–semiconductor–metal (MSM) UV photodetectors with $Al_{0.16}Ga_{0.84}N$/GaN heterostructures. Phys Status Solidi A, 2004, 201(12): 2686

[8] Hsu S H, Su Y K, Chang S J, et al. InGaAsN metal–semiconductor–metal photodetectors with modulation-doped heterostructures. IEEE Photonics Technol Lett, 2006, 18(3): 547

[9] Wu Zhengyun, Xin Xiaobin, Yan Feng, et al. Fabrication of MSM structure UV photodetector on 4H-SiC. Chinses Journal of Quantum Electronics, 2004, 21(2): 269

[10] ISE TCAD release 7.0 manual. Vol. 4a. ISE Integrated Systems Engineering AG, 2001

[11] Sze S M, Coleman D J, Loya A. Current transport in metal–semiconductor–metal (MSM) structures. Solid-State Electron, 1971, 14: 1209